ACS APPLIED MATERIALS & INTERFACES

Research Article

www.acsami.org

Enhanced Nonenzymatic Glucose-Sensing Properties of Electrodeposited $NiCo_2O_4$–Pd Nanosheets: Experimental and DFT Investigations

Kusha Kumar Naik,[†] Abhijeet Gangan,[‡] Brahmananda Chakraborty,*[,‡] Saroj K. Nayak,[†] and Chandra Sekhar Rout*[,†]

[†]School of Basic Sciences, Indian Institute of Technology, Bhubaneswar, Bhubaneswar 751013, Odisha, India

[‡]High Pressure and Synchrotron Radiation Physics Division, Bhabha Atomic Research Centre, Trombay, Mumbai 400085, India

Supporting Information

ABSTRACT: Here, we report the facile synthesis of $NiCo_2O_4$ (NCO) and $NiCo_2O_4$–Pd (NCO–Pd) nanosheets by the electrodeposition method. We observed enhanced glucose-sensing performance of NCO–Pd nanosheets as compared to bare NCO nanosheets. The sensitivity of the pure NCO nanosheets is 27.5 $\mu A\ \mu M^{-1}\ cm^{-2}$, whereas NCO–Pd nanosheets exhibit sensitivity of 40.03 $\mu A\ \mu M^{-1}\ cm^{-2}$. Density functional theory simulations have been performed to qualitatively support our experimental observations by investigating the interactions and charge-transfer mechanism of glucose on $NiCo_2O_4$ and Pd-doped $NiCo_2O_4$ through demonstration of partial density of states and charge density distributions. The presence of occupied and unoccupied density of states near the Fermi level implies that both Ni and Co ions in $NiCo_2O_4$ can act as communicating media to transfer the charge from glucose by participating in the redox reactions. The higher binding energy of glucose and more charge transfer from glucose to Pd-doped $NiCo_2O_4$ compared with bare $NiCo_2O_4$ infer that Pd-doped $NiCo_2O_4$ possesses superior charge-transfer kinetics, which supports the higher glucose-sensing performance.

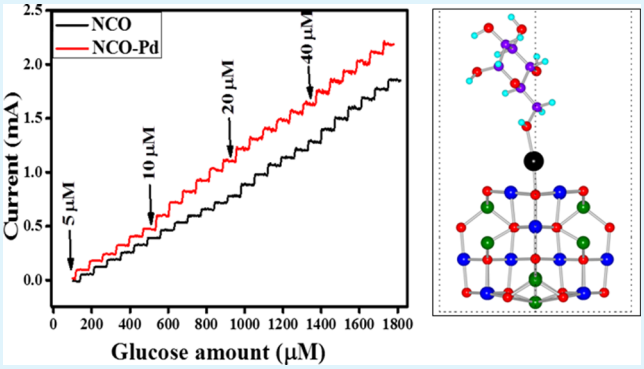

KEYWORDS: *spinel, biosensor, glucose sensor, nanosheets, computational study*

1. INTRODUCTION

The increasing demand for glucose sensors has driven tremendous effort for the development of reliable, high-precision, and cost-effective sensors because they possess opportunities for huge applications as an analytical device in the field of health care,[1,2] food, bioprocessing unit,[3,4] and biotechnology industries.[5] Simple and precise determination of glucose molecules is highly essential for excellent sensing devices.[6−8] Therefore, various nanomaterials comprising of metal oxides, nitrides, carbides, and chalcogenides possessing diverse morphologies have been employed as active materials for the fabrication of glucose-sensing devices.[9−12] Because glucose molecules are redox-active species, a number of redox-active materials have been investigated for their possible applications in glucose sensing.[13−15] It is well-known that transition-metal-based nanomaterials are highly electroactive, abundant, simple to synthesize, and cost-effective and thus are suitable candidates as effective glucose-sensing materials.[16−18]

Nickel cobalt oxide (NCO) is a redox-active material having an inverse spinel crystal structure. Because of the intrinsic vacant sites present within its crystal, it has the capacity to adsorb or replace the elements by dopants.[19,20] The effective catalytic and conductivity properties of the nanomaterials are easily tunable owing to which they find applications in glucose sensing. Furthermore, palladium has excellent electrocatalytic and biocatalytic properties. Hence, it is desirable to design a hybrid material by combining the electrochemical properties of $NiCo_2O_4$ and Pd to achieve enhanced glucose-sensing performance.[21,22]

Electrochemical detection of analytes is one of the most explored method because of its easy detection principle, compact instrumentation, and simple electrochemistry of the material.[23,24] Because glucose belongs to the group of intrinsically electroactive species, the electrochemical technique is more relevant for its effective detection compared with other techniques. This method further exhibits good sensitivity, selectivity, and better response time.[16,25] The nonenzymatic glucose sensors possess several advantages and their mechanism of detection toward glucose molecules is dealt with the redox reactions of the material.[19,20,26] In view of the above

Received: February 16, 2017
Accepted: June 23, 2017

DOI: 10.1021/acsami.7b02217
ACS Appl. Mater. Interfaces XXXX, XXX, XXX−XXX

advantages, we have performed and compared the glucose-sensing properties of the pure $NiCo_2O_4$ and $NiCo_2O_4$–Pd nanosheets electrodeposited on Ni foam. The synthesized material possesses glucose-sensing properties in the 5–90 μM linear range having sensitivities of 27.5 and 40.03 $\mu A\ \mu M^{-1}\ cm^{-2}$ for the $NiCoO_4$ and $NiCo_2O_4$–Pd nanosheets, respectively. Density functional theory (DFT) simulations have also been carried out to qualitatively support our experimental observations through analysis of the partial density of states (PDOS) and charge-density distribution. The reduction in the intensity of PDOS near the Fermi level for occupied p_x, p_y, and p_z orbitals of the O atom in the glucose molecule when it is attached to $NiCo_2O_4$ and Pd-doped $NiCo_2O_4$ indicates the charge transfer from the glucose molecule. Also, the presence of occupied and unoccupied density of states (DOS) for d orbital of Ni and Co ions indicates that both $NiCo_2O_4$ and $NiCo_2O_4$–Pd can act as charge-transfer media for efficient glucose sensing. Higher binding energy and larger charge transfer of glucose on Pd-doped $NiCo_2O_4$ show its superior electroactive properties toward glucose sensing as compared with bare $NiCo_2O_4$.

2. EXPERIMENTAL SECTION

2.1. Material Synthesis. The synthesis of $NiCo_2O_4$–Pd and bare $NiCo_2O_4$ were carried out in a three-electrode electrochemical setup by the chronoamperometric technique with the help of a standard potentiostat/galvanostat (PG262A, Techno Science Instruments, Bangalore, India). The first step is to clean the glass cell, Ni foam, Ag/AgCl reference electrode, and Pt wire counter electrode properly with ethanol and DI water. Then, 0.01 M of nickel nitrate hexahydrate was dissolved in 10 mL of DI water in a beaker. After that, 0.02 M of cobalt nitrate hexahydrate was thoroughly mixed to make a clear solution, followed by the addition of 1 mM of palladium chloride. The solution was stirred and sonicated for 15 min to make the complete dispersion of the dissolved precursors, and finally, the solution was transferred into the electrochemical glass cell. The three electrodes were placed in the glass cell, and the temperature of the electrolyte was maintained at 70 °C. A potential difference of −1.1 V was applied to the electrodes to initiate the deposition process. The deposition was executed for 180 s, and a dark green-colored film (0.5 × 0.6 cm^2) was grown on the surface of the Ni foam. Because of the high applied voltage and temperature, the ions from the dissolute precursors, that is, Ni^{2+}, Co^{2+}, Pd^{2+}, and OH^- react with each other triggering the nucleation to form $NiCo_2O_4$–Pd nanosheet composites. The nucleation, nanoparticle formation, and self-assembly of the nanoparticles on the Ni foam make homogeneous growth of the nanosheet morphology at a particular pattern. The dissolved OH^- acts as a source of oxygen and allows the hydrolysis process to grow the nanostructures. As-grown thin film was washed several times to remove the impurities and unreacted ions followed by vacuum drying at room temperature. The dried film was annealed at 400 °C for 6 h to oxidize the hydroxides present in the thin film, and finally, a black-colored thin film was obtained for characterization. The schematic representation and image of the deposition process of the material are implicated in Scheme 1. Similar precursors and synthesis process were followed to grow pure $NiCo_2O_4$ nanosheets for the comparative study of glucose-sensing performance of $NiCo_2O_4$–Pd and bare $NiCo_2O_4$ nanosheets.

2.2. Material Characterization. The phase and crystalline nature of the as-synthesized materials were characterized by X-ray diffraction (XRD) analysis [Bruker D8 ADVANCE diffractometer using Cu Kα radiation (λ = 1.54184 Å)]. Morphology and composition of the materials were determined by a field-emission scanning electron microscopy (FESEM, MERLIN Compact with GEMINI I electron column, Zeiss Pvt. Ltd, Germany) instrument equipped with energy-dispersive X-ray analysis (EDAX). Transmission electron microscopy (TEM), high-resolution transmission electron microscopy (HRTEM), and electron diffraction patterns were collected by a JEM-2100 transmission electron microscope with an acceleration voltage of 200 kV. All X-ray photoelectron spectroscopy (XPS) measurements were recorded in VG Microtech, England (MultiLab, ESCA-3000. Sr. no—8546/1, MultiLab) under ultra-high vacuum condition.

Scheme 1. Schematic of the Electrodeposition Method with Photograph of Ni Foam: (A) before and (B) after Electrodeposition. Photographs of (C) NCO and (D) NCO–Pd Nanosheets after Annealing

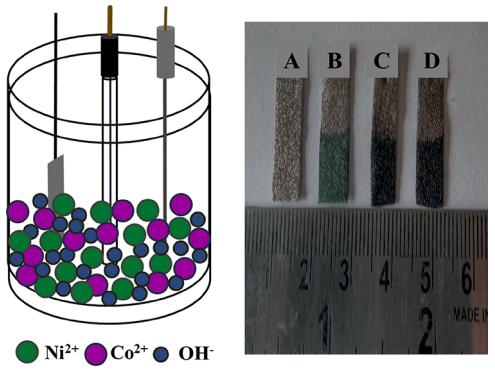

2.3. Electrochemical Measurement. To study the sensing performance of the synthesized materials, electrochemical experiments such as cyclic voltammetry (CV) and chronoamperometry (CA) were executed in a three-electrode glass cell connected to an electrochemical workstation (PG262A, Techno Science Instruments, Bangalore, India) taking 0.1 M of NaOH solution as the electrolyte. In the three-electrode setup, NCO or NCO–Pd nanosheets deposited on Ni foam, Pt wire, and Ag/AgCl electrodes were used as the working electrode, counter electrode, and reference electrode, respectively. For CV experiments, 10 mL of NaOH was taken in the glass cell and then glucose was pipetted into the solution at different molar concentrations to observe the current response of the material. Similarly, for CA experiment, 140 mL of NaOH solution was taken in the glass cell and then three electrodes were connected, and the solution was stirred at a constant speed of 675 rpm. Finally, a constant potential of 0.4 V was supplied to the three electrodes, and the analytes were added to the rotating solution at different molar concentrations to observe the sensing response of the materials. The interference study was executed by performing CA experiments in the presence of different interfering species such as ascorbic acid, uric acid, dopamine, lactic acid, and so forth.

3. RESULTS AND DISCUSSION

3.1. Characterization of the Synthesized Materials. The morphology of the as-synthesized pure NCO and NCO–Pd nanosheets is depicted in Figure 1. Figure 1A,B shows low and high magnification images of pure NCO grown in a particular fashion having a nanosheet structure and interconnected with each other. The width and the length of the nanosheets are in the range of 25–45 nm and ∼1–2 μm, respectively, having homogeneous orientation and distribution with high stability containing numerous redox-active sites desirable for efficient oxidation of glucose molecules. Similarly, Figure 1C,D shows the morphology of NCO–Pd nanosheets that possess a similar nanosheet-like structure but are interconnected and fused with each other to form a bunch of nanosheets. The length of the individual NCO–Pd nanosheets is approximately in the 30–50 nm range, and the length of the bunch of nanosheets is in the 0.5–1.0 μm range. The side views of the pure NCO and NCO–Pd nanosheets are provided in Figure S1. The growth direction and orientation of bunched nanosheets are uniform and homogeneous everywhere. Because

DOI: 10.1021/acsami.7b02217
ACS Appl. Mater. Interfaces XXXX, XXX, XXX–XXX

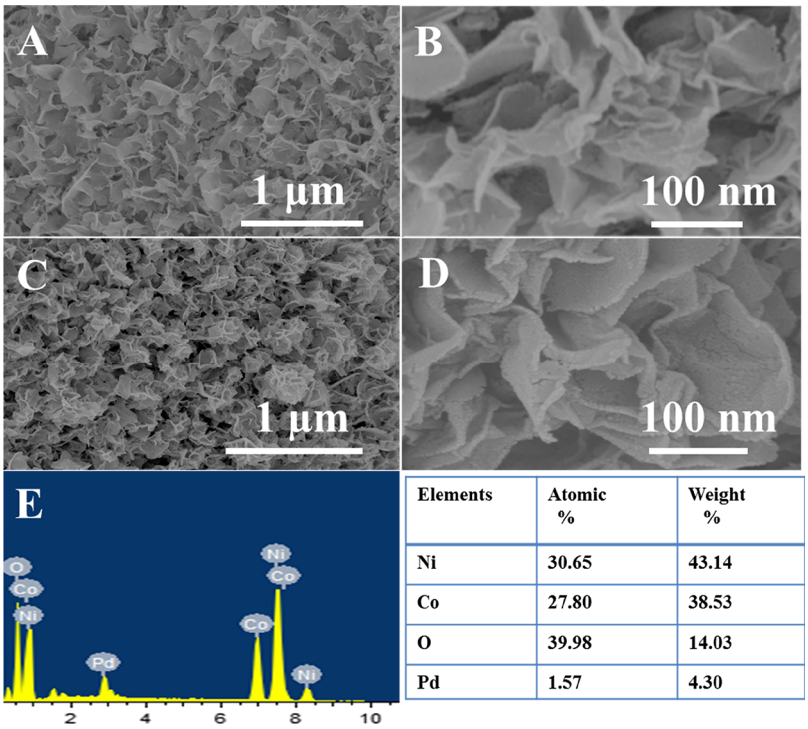

Elements	Atomic %	Weight %
Ni	30.65	43.14
Co	27.80	38.53
O	39.98	14.03
Pd	1.57	4.30

Figure 1. (A) Low and (B) high magnification FESEM images of pure NCO nanosheets. (C) Low and (D) high magnification FESEM images of NCO−Pd nanosheets. (E) EDAX spectrum with percentage of elements present in the electrodeposited NCO−Pd nanosheets.

of these reasons, there is an enhancement in the effective surface area, surface to volume ratio, and electrocatalytic active sites of NCO−Pd nanosheets. The composition of the nanostructure has been investigated through the EDX spectra, as shown in Figure 1E. The atomic percentages of Ni, Co, O, and Pd are 30.65, 27.8, 39.98, and 1.57, respectively. Because we have used the films of the materials electrodeposited on the Ni foam for the scanning electron microscopy and EDAX analyses, the atomic ratio of Ni/Co is not consistent with the stoichiometric ratio of $NiCo_2O_4$. The low content of "Pd" element without agglomeration and uniform distribution in the $NiCo_2O_4$ matrix enhances the conductivity and electrocatalytic activity of the material. The distribution and the uniformity of the individual elements present in the nanosheets are verified by the electron mapping spectra shown in Figure S2.

The purity and phase of the materials are characterized by the XRD, and the obtained patterns are depicted in Figures 2 and S3. The peaks (220), (311), (400), (511), (620), and (440) are indexed to pure $NiCo_2O_4$ having a cubic crystal structure with lattice parameter $a = b = c = 8.11$ Å (JCPDS: 20-0781). No other stray peaks are observed, which demonstrates the pure phase quality of the synthesized material. In the case of NCO−Pd nanosheets, a low intense peak corresponding to Pd is observed at 40.23°, confirming the presence of "Pd" elements in the nanosheets.[21,22] The peaks are distinct and sharp, which characterize the crystalline nature of the synthesized materials. To obtain more detailed information on the elemental composition and oxidation states of the elements present in the NCO−Pd nanosheets, we have performed the XPS analysis, and the data are shown in Figure S4. The survey spectrum (Figure S4A) indicates the presence of Ni, Co, O, and Pd without any other impurities. By using the Gaussian fitting method, the Ni 2p is fitted to two spin−orbit doublets, which is characteristic of Ni^{2+} and Ni^{3+} and two shake-up satellite peaks, as shown in Figure S4B. The fitted peaks at 855.41 and 872.73 eV are assigned to Ni^{2+} and Ni^{3+}, respectively.[27] The satellite peaks at around 879.99 and 861.53 eV are two shake-up-type peaks of nickel at high-energy side of the Ni $2p_{1/2}$ and Ni $2p_{3/2}$ edge, respectively.[28] Figure S4C represents the Co 2p spectra, with two peaks positioned at 779.92 and 795.81 eV that are attributed to the Co $2p_{3/2}$ and $2p_{1/2}$, respectively. The gap between two satellite peaks is about 15.89 (spin−orbit splitting), which is in accordance with the previous reports of Co-oxides.[29,30] Figure S4D represents the Pd 3d spectra with peaks at 342.71 and 337.14 eV, which are assigned to $3d_{3/2}$ and $3d_{5/2}$ states, respectively.[31,32] Figure S4E presents the O 1s spectrum where the correspondence peak is positioned at 529.76 eV, which is in accordance with the metal−oxygen bond, whereas the component at 531.94 eV is associated with oxygen ions of OH^- groups. The presence of O 1s spectrum indicates that the surface of the $NiCo_2O_4$ material is hydroxylated to some extent as a result of either surface oxides or the substitution of an oxygen atom at the surface by a

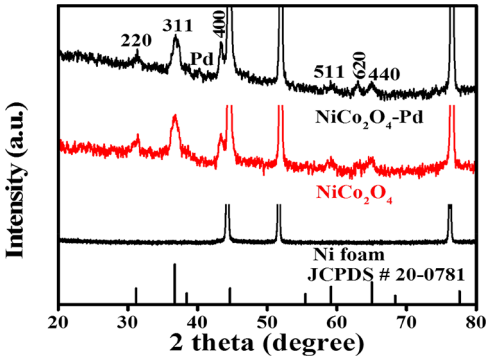

Figure 2. Comparison of XRD spectra of NCO and NCO−Pd nanosheets electrodeposited on the Ni foam substrate.

DOI: 10.1021/acsami.7b02217
ACS Appl. Mater. Interfaces XXXX, XXX, XXX−XXX

hydroxyl group.[33] These results show that the chemical composition of $NiCo_2O_4$–Pd nanosheets contain Ni^{2+}, Ni^{3+}, Co^{2+}, Co^{3+}, Pd^{3+}, and Pd^{5+}, which are in good agreement with the literature for $NiCo_2O_4$–Pd materials.[34] The solid redox couple of Ni^{2+}/Ni^{3+} and Co^{2+}/Co^{3+} can afford enough active sites for glucose oxidation, which is one of the important factors contributing to the high electrocatalytic performance of $NiCo_2O_4$ nanosheets. To know the exact morphology of the synthesized material, TEM analysis of the NCO–Pd nanosheet sample was performed, as shown in Figure 3. The images

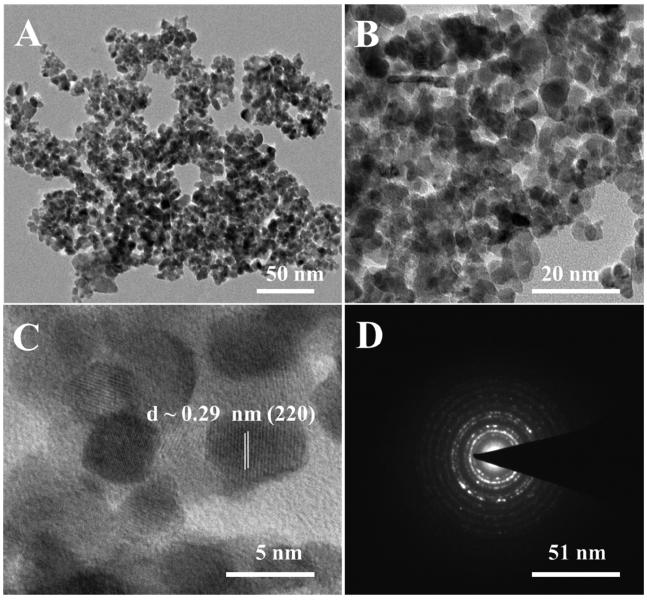

Figure 3. (A,B) TEM images, (C) HRTEM image, and (D) SAED pattern of NCO–Pd nanosheets.

clearly reveal the particle nature of the material. Nanosheets are formed when these nanoparticles are self-assembled. The lattice fringe of the nanosheets is 0.29 nm, which corresponds to the (220) planes, and is in very good agreement with the XRD data. The selected area electron diffraction (SAED) pattern of the NCO–Pd clearly reveals the polycrystalline nature of the NCO–Pd nanosheets.

3.2. Electrocatalytic Oxidation of Glucose. The CV study of both the NCO and NCO–Pd nanosheets was carried out with and without glucose analytes in 0.1 M of NaOH solution in the potential range of 0–0.7 V at a scan rate of 20 mV s^{-1}. Figure 4A clearly specifies the spectrum of the glucose-sensing activity for both without and with 100 μM glucose inside of the solution, and the distinguished peak obtained at 0.5 V is assigned as the oxidation peak of pure NCO.[35−37] The detailed glucose-sensing mechanism of the NCO nanosheets has been explained in our previous study.[38−40] Here, we outline the governing reactions

$$NiCo_2O_4 + OH^- + H_2O \leftrightarrow NiOOH + 2CoOOH + e^- \quad (1)$$

$$\text{Glucose } (C_6H_{12}O_6) \rightarrow \text{gluconolactone } (C_6H_{10}O_6) + 2H^+ + 2e^- \quad (2)$$

During the CV experiment, Ni and Co species present in the dissolved NiOOH and CoOOH compounds oxidize and reduce simultaneously, as described in eq 1. When we dropped the glucose molecules, they dissociate and convert to gluconolactone by giving up two electrons into the solution (eq 2). Because of the oxidation of glucose molecules and reduction of ion species, glucose molecules are detected by the material. The redox of Ni and Co ions and glucose molecules occurs simultaneously in the same potential range, but the rate of oxidations of Ni and Co ions present on the electrode surface determines the rate of detection of glucose molecules. Thus, the detection of the glucose molecule is the intrinsic electrochemical activity of the material, and the rate of detection can be enhanced by engineering the morphology, tuning the composition of the materials, designing hybrid materials, and controlling other parameters such as pH, the molarity of the aqueous solution, and the substrate.

No other peaks are observed in the CV experiments, which suggest that the presence of "Pd" elements inside of the nanostructure has no individual electrochemistry in the oxidation and reduction of the glucose molecules. It has a combined effect with Ni and Co ions toward oxidation of glucose molecules. Therefore, the oxidation peak current (I_p) of the NCO–Pd material shows more enhanced current values (I_{ap}) than the oxidation peak current (I_{ap}) of pure NCO. The CV experiments at different concentrations of glucose and at different scan rates have been included in Figure S5. Figure 4B demonstrates the electrocatalysis of the materials with a regular increase in the glucose molarity (100–1000 μM) in the solution, and the linear nature of glucose oxidation has been observed. The oxidation peak current at each step of addition of glucose solution shows linear variation in both the NCO–Pd and NCO nanosheets, which is essential for the efficient glucose sensor.

3.2.1. Glucose Oxidation and Its Determination. The chronoamperometric study of the material was executed at 0.4 V, and glucose solution was added to the rotating solution at different molar concentrations with a regular interval of 70 s, producing a staircase-like graph as depicted in Figure 4C. Although the nature of the graph of the two materials is the same, higher current value strongly infers the advantage of the doped "Pd" element in the composite. Figure 4D defines the calibration graph of NCO–Pd and NCO nanosheets, which are almost similar in nature but possess two types of linear ranges: 5–90 and 170–450 μM, respectively. The calculated sensitivity of the pure NCO and NCO–Pd nanosheets was found to be 27.5 and 40.03 μA μM^{-1} cm^{-2}, respectively, in the 5–90 μM linear range and, similarly, 8.53 and 8.23 μA μM^{-1} cm^{-2}, respectively, in the 170–450 μM linear range.

The limit of detection of the materials was calculated in different linear ranges by the following formula

$$\text{LOD} = \frac{3 \times \text{SD}}{m}$$

where "SD" is the standard deviation of the materials and "m" is the slope of the calibration graph. The SD of pure NCO and NCO–Pd is 0.006817 and 0.001150, respectively. The calculated limit of detection was found to be 2.46 μM for pure NCO and 0.28 μM for NCO–Pd nanosheets in the range of 5–90 μM (see Figure S6 for the detailed glucose-sensing performance of NCO–Pd nanosheets).

3.2.2. Selectivity, Stability, and Reproducibility. The selectivity of the nonenzymatic glucose sensor is depicted in Figure S7A. The interference study of NCO–Pd nanosheets confirms the high selectivity toward glucose molecules, and it shows the partial interfering effect toward dopamine. To check

DOI: 10.1021/acsami.7b02217
ACS Appl. Mater. Interfaces XXXX, XXX, XXX–XXX

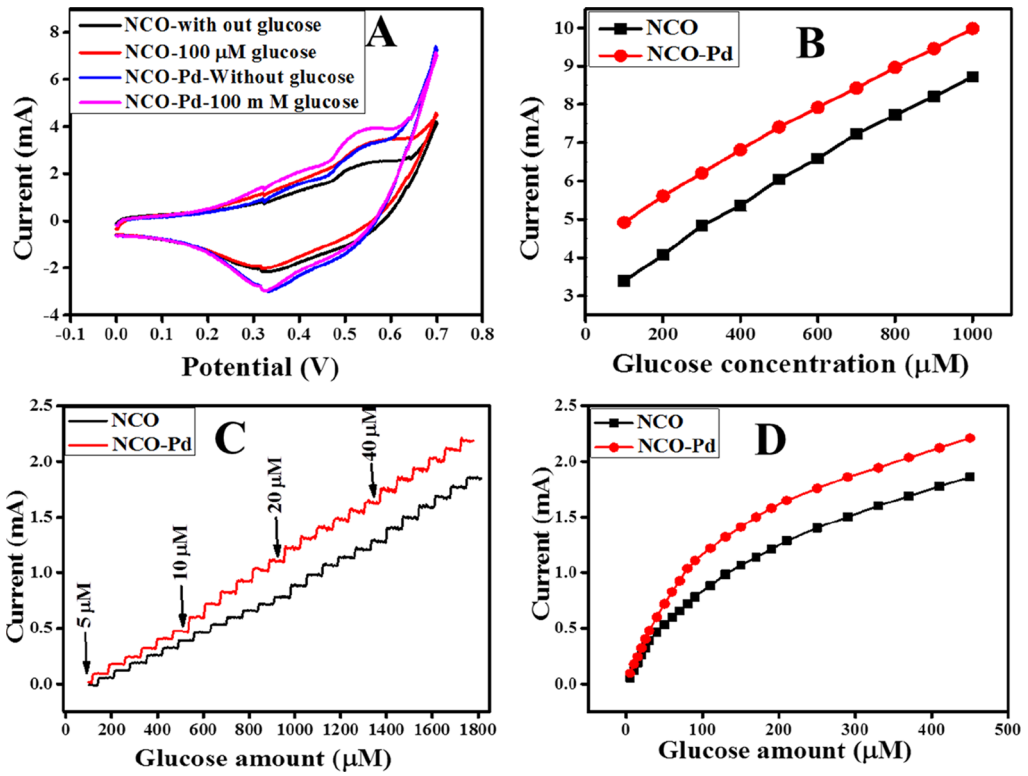

Figure 4. (A) CV curves of NCO and NCO−Pd nanosheets executed in 0.1 M of NaOH solution and (B) change in oxidation peak current with respect to glucose concentration. (C) *I*−*t* curves and (D) calibration curves of NCO and NCO−Pd nanosheets.

the stability of the glucose-sensing performance, the CA experiment was performed at 0.4 V in the presence of 30 μM glucose molecules for 3600 s and the applied voltage of 0.4 V was maintained for the entire period, as shown in Figure S7B. To check the reproducibility, five individual electrodes were tested and only 5% deviation in the glucose-sensing performance was observed. The glucose-sensing performance of the present materials is compared with other 2D nanosheet materials reported in the literature, and it is presented in Table 1. The enhanced sensing performance of the $NiCo_2O_4$−Pd hybrid nanosheets justifies their suitability for glucose-sensing applications.

Table 1. Comparison of Glucose-Sensing Performance of NCO−Pd Nanosheets with Other 2D Nanosheet Materials Reported in the Literature

electrode	sensitivity (μA μM^{-1} cm^{-2})	linear range (μM)	LOD (μM)	reference
$CuCo_2O_4$	3.625	up to 320	5	41
$NiCo_2S_4$	5.14	1−664	1.2	42
$MnCo_2O_4$	8.2	20−100	3.2	43
$NiCo_2O_4$	27.5	5−90	2.46	present work
$NiCo_2O_4$−Pd	40.03	5−90	0.28	present work

4. THEORETICAL INVESTIGATIONS

To support the experimental observations, we have also performed theoretical investigations to get insight into the interaction and charge-transfer mechanism of glucose and $NiCo_2O_4$ and Pd-doped $NiCo_2O_4$ through electronic structure calculations.

4.1. Computational Details. The VASP package is used to carry out the first principle calculations.[44−47] PAW-based pseudo-potentials have been used for Ni, Co, Pd, C, O, and H with PBE as the exchange−correlation functional.[48] The semicore p states are included for Ni, Co, and Pd atoms. The cutoff energy is taken to be 500 eV, and the Brillouin zone is sampled using a Monkhorst−Pack[49] mesh of 8 × 8 × 1 and 8 × 8 × 8 *k*-points for surface and bulk geometries, respectively. All calculations are performed within the spin-polarized DFT framework. The initial structure of α-glucose was optimized in a cubic cell of lattice parameter 20 Å, which is large enough to avoid any periodic interactions, as α-glucose is a molecule, the Brillouin zone was sampled using only gamma points. The convergence criterion for Hellmann−Feynman forces and total energy is set to 0.01 eV/Å and 10^{-6} eV, respectively. As DFT does not incorporate the weak dispersion forces, the optimizations and total energy calculations were repeated using Grimme's DFT-D2,[54] which uses a pairwise force field for describing the van der Waals (vdW) interactions.

4.2. Interaction of Glucose on $NiCo_2O_4$. First, we have relaxed the bulk $NiCo_2O_4$ with an inverse spinel structure, and the optimized lattice parameter comes out to be 8.09 Å, in agreement with the experimental value of 8.11 Å.[50] As seen in Figure 5, Ni ions are octahedrally coordinated with the O ions, whereas Co ions are tetrahedrally coordinated with the O ions. Computed Ni−O and Co−O bond lengths are 1.93 and 1.92 Å, respectively. The DOS presented in Figure 5 shows that the bulk $NiCo_2O_4$ is half-metallic in nature with DOS only in the lower spin channel at the Fermi level, which is consistent with the literature.[51] The matching of the lattice parameters and DOS (half-metallic characteristics) of $NiCo_2O_4$ gives confidence regarding the accuracy of the simulation procedures and validity of the exchange−correlation functional. As the

DOI: 10.1021/acsami.7b02217
ACS Appl. Mater. Interfaces XXXX, XXX, XXX−XXX

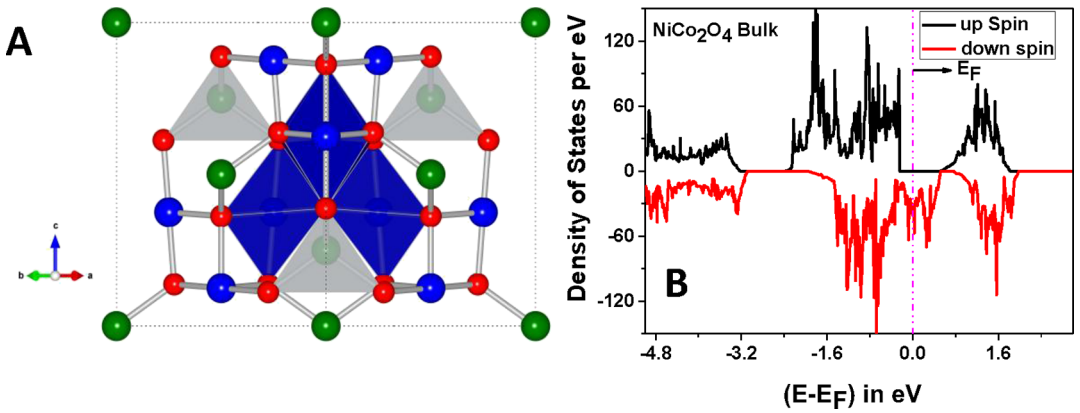

Figure 5. DFT-optimized structure of inverse spinel structure of $NiCo_2O_4$ (A) with Ni in octahedral and Co in tetrahedral environment of surrounding oxygen atoms as shown in the polyhedral. (B) Total DOS for bulk $NiCo_2O_4$ revealing its semimetallic nature.

experiment has been carried out on $NiCo_2O_4$ (also with Pd-doped) nanosheets, we have done further calculations on the $NiCo_2O_4$ surface, as shown in Figure 6. Figure S8 depicts the DOS for the $NiCo_2O_4$ surface and glucose attached on the $NiCo_2O_4$ surface. We can notice that there are occupied states at and around the Fermi level and also unoccupied states above the Fermi level for the $NiCo_2O_4$ surface, which may favor $NiCo_2O_4$ as communicative media for charge transfer. To get insight into the orbital charge distribution for Ni and Co d orbital, PDOS has been displayed in Figure 7. For Ni d orbital, charges are mostly in dz^2 and $dx^2 - y^2$, whereas there appear unoccupied states in d_{yz}, d_{xz}, and d_{xy} suborbitals. For Co d orbital, charge stays mostly in d_{xz}, d_{yz}, and d_{z^2} suborbital and there are more unoccupied states near the Fermi level in $d_{x^2-y^2}$, d_{z^2}, and d_{xz} suborbitals. The presence of occupied and unoccupied DOS near the Fermi level signifies that both Ni and Co transfer the charge from glucose by participating in the redox reaction. As the system is magnetic with a magnetic moment of 1.16 μ_B per cation, the charge transfer may be more because the magnetic system has better charge-transfer mechanism.[52,53] From Bader charge analysis, we can mention that in $NiCo_2O_4$ oxygen atoms gain around 1.0*e* charge from Ni and Co.

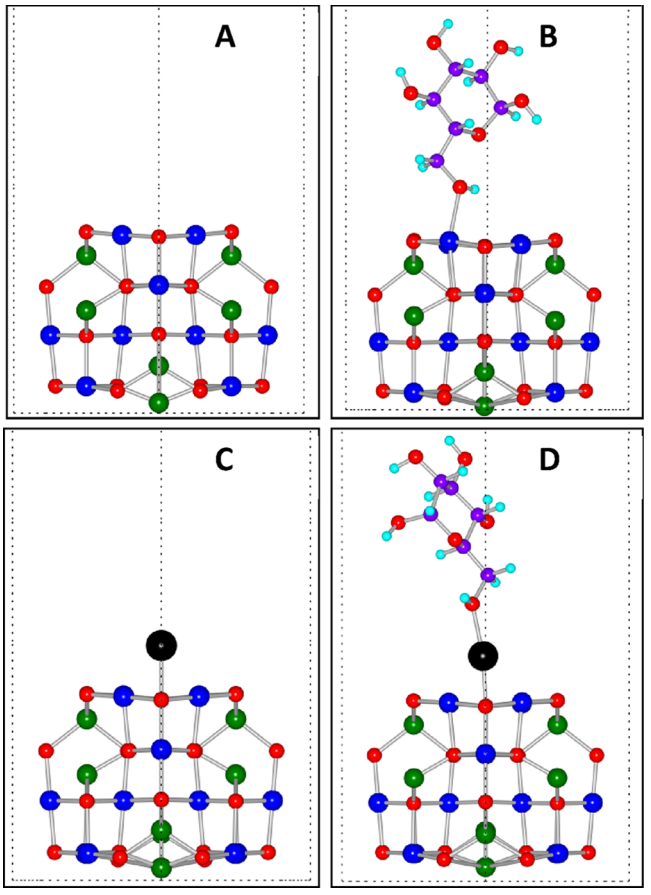

Figure 6. DFT optimized structures of (A) $NiCo_2O_4$, (B) $NiCo_2O_4$ + α-glucose, (C) $NiCo_2O_4$+ Pd, and (D) $NiCo_2O_4$ + Pd + α-glucose. Here, the blue, green, red, purple, black, and cyan represent Co, Ni, O, C, Pd, and H atoms, respectively.

Next, we introduced α-glucose molecule on the $NiCo_2O_4$ surface and allowed the system to relax. In the presence of a glucose molecule, the oxygen atoms gain charge of around 1.75*e* from the bonded hydrogen and carbon atoms. The binding energy of glucose on the $NiCo_2O_4$ surface was computed using the formula

$$E_b(Y) = E(NCO + Glu) - E(NCO) - E(Glu)$$

where $E(NCO)$ is the energy of $NiCo_2O_4$, $E(Glu)$ is the energy of the single glucose molecule, and $E(NCO + Glu)$ is the energy of NCO + glucose system. The computed binding energy is −0.31 eV; the negative binding energy refers that the binding of glucose on the $NiCo_2O_4$ surface is energetically favorable. With the inclusion of vdW interaction, the binding energy of glucose on NCO becomes stronger with a binding energy of −0.57 eV. Therefore, the glucose is bonded strongly on the $NiCo_2O_4$ surface with a bond length of 2.24 Å between O of glucose and nearest Co of $NiCo_2O_4$. To check the stability of the $NiCo_2O_4$ + glucose system, we have carried out ab initio molecular dynamics (MD) simulation at 300 K and the snapshot obtained at 300 K as displayed in Figure S9A confirms that the system is stable and there is no noticeable movement of the atoms.

We can see from Figure S8 that in the case of $NiCo_2O_4$ + glucose, the intensity of DOS in the valence band is higher compared with $NiCo_2O_4$ because of the charge coming from glucose. Figure 8 displays the PDOS of p orbital of the oxygen atom of the glucose when it is in the glucose molecule, attached to the $NiCo_2O_4$ surface and attached to the Pd-doped $NiCo_2O_4$ surface. When glucose is attached to $NiCo_2O_4$ surface, there is a charge transfer from O p orbital. We can notice from PDOS

DOI: 10.1021/acsami.7b02217
ACS Appl. Mater. Interfaces XXXX, XXX, XXX−XXX

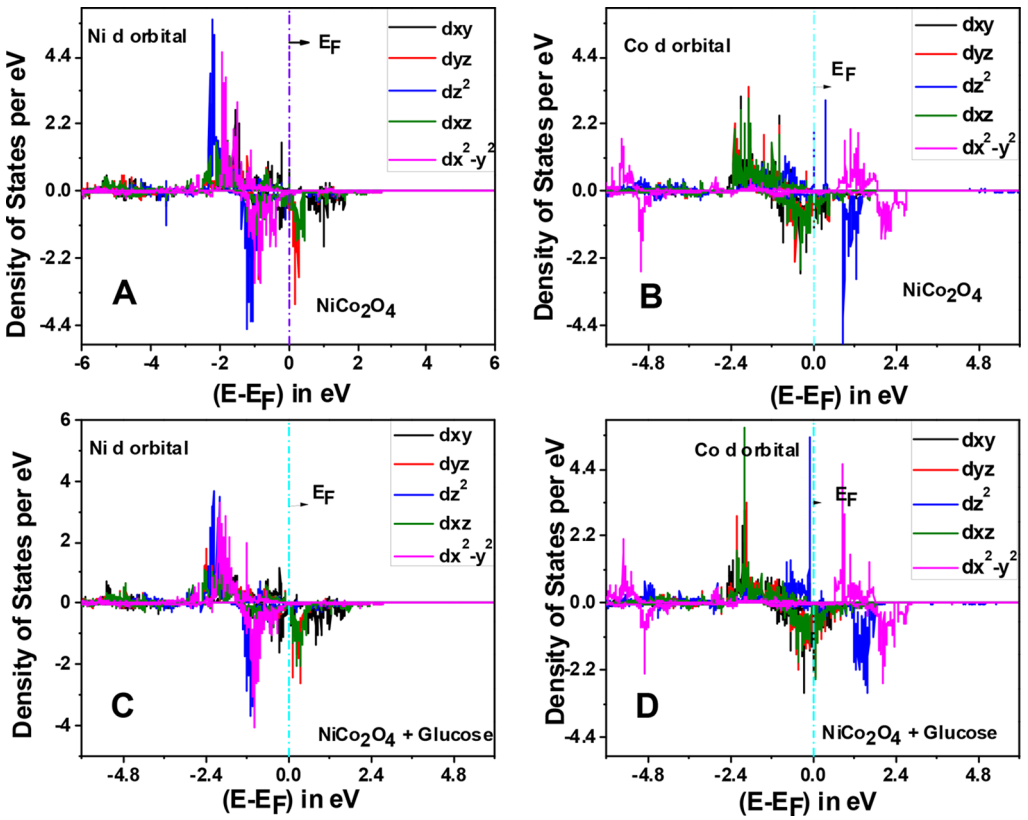

Figure 7. Comparison of PDOS of (A,B) Ni and Co d orbitals in $NiCo_2O_4$ and (C,D) $NiCo_2O_4$ + α-glucose.

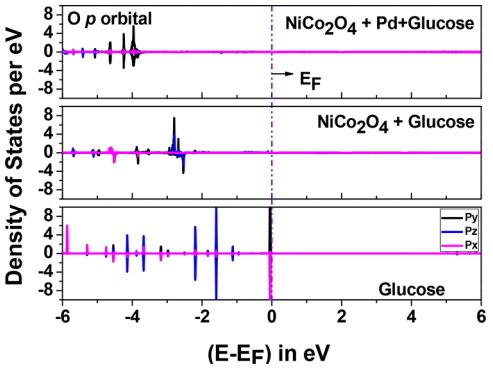

Figure 8. PDOS of oxygen p orbitals in α-glucose, $NiCo_2O_4$ + α-glucose, and $NiCo_2O_4$ + Pd + α-glucose.

plot of O p orbital as presented in Figure 8 that the intensity of PDOS for occupied p_x, p_y, and p_z orbitals near the Fermi level has reduced when it is attached to the $NiCo_2O_4$ surface. Also, most of the occupied states are now located deep in the valance band, indicating the charge transfer from the top of the valance band. There also appear few empty states above the Fermi level. There is also little bit spin splitting in p orbitals of O atoms because of the presence of magnetic $NiCo_2O_4$. Because there is charge transfer from glucose to $NiCo_2O_4$, the bonding is ionic in nature. The strong interaction of glucose on $NiCo_2O_4$ and charge transfer may indicate that glucose is getting oxidized. Here, we mention that in the experiment, the Ni and Co are already oxidized, so the charge transfer from glucose in the actual case will be more.

4.3. Interaction of Glucose on Pd-Doped $NiCo_2O_4$. To qualitatively investigate the glucose-sensing capability of Pd-doped $NiCo_2O_4$, we introduce one Pd atom 2.5 Å above the surface and allow the system to relax. The Pd atom is bonded with a binding energy of −3.75 eV and makes a bond of 2.01 Å with the nearest Co atom as shown in the optimized structure in Figure 6C. When glucose is introduced, it is bonded with Pd with a binding energy of −0.48 eV and makes bond with the Pd atom having a bond length of 2.04 Å. When vdW interaction is incorporated, the binding energy increases to −0.73 eV. Therefore, we can notice that in the presence of Pd, glucose is bonded strongly on the $NiCo_2O_4$ surface compared with the case of without Pd. To check the stability of the $NiCo_2O_4$ + Pd + glucose system, we have performed Ab initio MD simulation at 300 K and the structural snapshot obtained at 300 K as presented in Figure S9B confirms that the system is quite stable and there is no deformation or noticeable movement of the atoms.

Figure S10 displays the total DOS for isolated Pd, Pd-doped $NiCo_2O_4$, and glucose attached on Pd-doped $NiCo_2O_4$. For isolated Pd, there are occupied states near the Fermi level, which appear in the DOS of Pd-doped $NiCo_2O_4$, making Pd-doped $NiCo_2O_4$ more conducting compared to only $NiCo_2O_4$. Therefore, in the presence of Pd, oxidation of Ni and Co ions would be more favorable, which supports higher sensitivity of Pd-doped $NiCo_2O_4$ compared to only $NiCo_2O_4$ as observed in the experiment. In order to see the spatial distribution of charge density in Figure 9, we have presented the contour plot of charge density of glucose and charge density difference between $NiCo_2O_4$ + Pd + α-glucose and α-glucose. The blue region is the charge-depleted region, and the red region is the charge-rich region. It is clear from the plot that there is charge transfer from glucose to the Pd as the charge-loss (blue) region

DOI: 10.1021/acsami.7b02217
ACS Appl. Mater. Interfaces XXXX, XXX, XXX−XXX

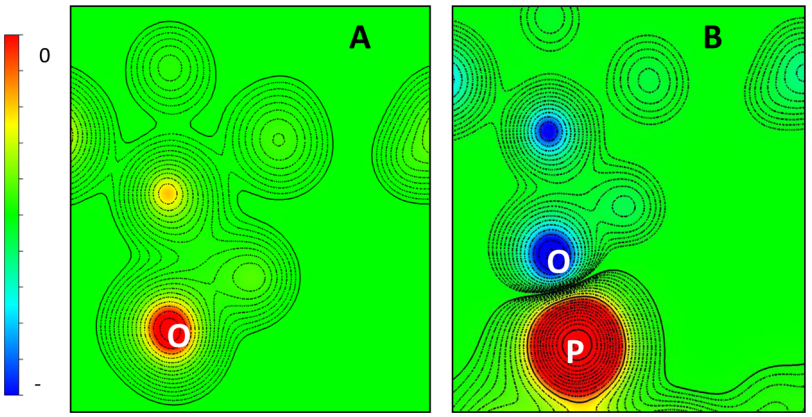

Figure 9. (A) Contour plot of charge density of glucose and (B) charge-density difference between $NiCo_2O_4$ + Pd + α-glucose and α-glucose. The blue region is the charge-depleted region, and red region is the charge-rich region.

corresponds to the bonded O atom of glucose, whereas the charge-gain (red) region corresponds to the bonded Pd atom.

4.4. Practical Applications of Glucose Sensors in Real Samples. Under the optimal experimental condition, the quantitative determination of glucose present in human blood serum was performed on the developed NCO−Pd sample. At first, the blood serum was tested by an analytical kit (GLUCOCARD 01-Mini) and the results are compared with the data obtained using our sensor. The determined results of the sample are provided in Figure S11 and Table S1, which are accurate and creditable, indicating that the proposed non-enzymatic glucose sensor can be utilized for the detection of glucose in human blood serum.

5. CONCLUSIONS

We have demonstrated the facile approach for the synthesis of pure NCO and NCO−Pd nanosheets by the electrodeposition method. The synthesized materials possess nanosheet morphology with enormous electrocatalytic and biocatalytic active centers on the surface. Therefore, the electrons generated through oxidation of glucose molecules are absorbed by these active centers and the glucose content is detected. The sensitivity of the pure NCO nanosheets is 27.5 μA μM^{-1} cm^{-2}, whereas NCO−Pd nanosheets exhibit sensitivity of 40.03 μA μM^{-1} cm^{-2}. The interaction and charge-transfer mechanism of glucose on $NiCo_2O_4$ and $NiCo_2O_4$−Pd have also been investigated through electronic structure simulations to strengthen our experimental observations. The DOS analysis predicts that the existence of occupied and unoccupied DOS near the Fermi level for d orbital of both Ni and Co ions makes $NiCo_2O_4$ and Pd-doped $NiCo_2O_4$ as superior charge-transfer media for glucose sensing. From the contour plot of charge-density distribution, it is seen that O of glucose, which is bonded to Pd atom corresponds to the charge-loss (blue) region, whereas Pd corresponds to the charge-gain region, implying charge transfer from glucose to Pd-doped $NiCo_2O_4$ (as well as bare $NiCo_2O_4$). As $NiCo_2O_4$ (also Pd-doped $NiCo_2O_4$) is magnetic with a magnetic moment of 1.16 μ_B per cation, it possesses superior charge-transfer kinetics compared with nonmagnetic systems. Thus, the synthesized materials are good for glucose sensors and can be recommended for industrial applications.

■ ASSOCIATED CONTENT

Supporting Information

The Supporting Information is available free of charge on the ACS Publications website at DOI: 10.1021/acsami.7b02217.

Elemental mapping, comparative glucose-sensing performance of pure NCO and NCO−Pd nanosheets, spin-polarized total DOS for the $NiCo_2O_4$ surface, Ab initio MD simulation snapshot at 300 K for $NiCo_2O_4$ + glucose and $NiCo_2O_4$ + Pd + glucose, and comparison of the PDOS of Ni and Co d orbitals in $NiCo_2O_4$ (PDF)

■ AUTHOR INFORMATION

Corresponding Authors

*E-mail: brahma@barc.gov.in (B.C.).

*E-mail: csrout@iitbbs.ac.in, csrout@gmail.com (C.S.R.).

ORCID

Chandra Sekhar Rout: 0000-0003-4380-5549

Notes

The authors declare no competing financial interest.

■ ACKNOWLEDGMENTS

C.S.R. would like to thank DST (Government of India) for the Ramanujan fellowship (grant no. SR/S2/RJN-21/2012). This work was supported by the DST-SERB Fast-track Young scientist (grant no. SB/FTP/PS-065/2013), UGC-UKIERI thematic awards (grant no. UGC-2013-14/005), and BRNS-DAE (grant no. 37(3)/14/48/2014-BRNS/1502). Also, part of this work is supported by the Indo-US Science and Technology Forum (IUSSTF) through a joint INDO-US centre grant and Ministry of Human Resources Development (MHRD), India, through a center of excellence grant. B.C. would like to thank Dr. N. K. Sahoo for support and encouragement. B.C. would also like to thank the staff of BARC computer division for supercomputing facility.

■ REFERENCES

(1) Pantelopoulos, A.; Bourbakis, N. G. A Survey on Wearable Sensor-Based Systems for Health Monitoring and Prognosis. *IEEE Trans. Syst. Man Cybern. C Appl. Rev.* **2010**, *40*, 1−12.

(2) Brown, S. J. Modular Microprocessor-Based Health Monitoring System. U.S. Patent 5,899,855, May 4, 1999.

(3) Wagner, G. *Food Biosensor Analysis*; CRC Press, 1993; Vol. *60*.

(4) Neethirajan, S.; Jayas, D. S. Nanotechnology for the Food and Bioprocessing Industries. *Food Bioprocess Technol.* **2011**, *4*, 39−47.

DOI: 10.1021/acsami.7b02217
ACS Appl. Mater. Interfaces XXXX, XXX, XXX−XXX

(5) Wang, Y.; Li, Z.; Wang, J.; Li, J.; Lin, Y. Graphene and Graphene Oxide: Biofunctionalization and Applications in Biotechnology. *Trends Biotechnol.* **2011**, *29*, 205−212.
(6) Oliver, N. S.; Toumazou, C.; Cass, A. E. G.; Johnston, D. G. Glucose Sensors: A Review of Current and Emerging Technology. *Diabetic Med.* **2009**, *26*, 197−210.
(7) Lakshmi, D.; Bossi, A.; Whitcombe, M. J.; Chianella, I.; Fowler, S. A.; Subrahmanyam, S.; Piletska, E. V.; Piletsky, S. A. Electrochemical Sensor for Catechol and Dopamine Based on a Catalytic Molecularly Imprinted Polymer-Conducting Polymer Hybrid Recognition Element. *Anal. Chem.* **2009**, *81*, 3576−3584.
(8) Chen, S.; Yuan, R.; Chai, Y.; Hu, F. Electrochemical Sensing of Hydrogen Peroxide Using Metal Nanoparticles: A Review. *Microchim. Acta* **2013**, *180*, 15−32.
(9) Rahman, M. M.; Ahammad, A. J. S.; Jin, J.-H.; Ahn, S. J.; Lee, J.-J. A Comprehensive Review of Glucose Biosensors Based on Nanostructured Metal-Oxides. *Sensors* **2010**, *10*, 4855.
(10) Robinson, J. T.; Perkins, F. K.; Snow, E. S.; Wei, Z.; Sheehan, P. E. Reduced Graphene Oxide Molecular Sensors. *Nano Lett.* **2008**, *8*, 3137−3140.
(11) Qiu, R.; Zhang, X. L.; Qiao, R.; Li, Y.; Kim, Y. I.; Kang, Y. S. CuNi Dendritic Material: Synthesis, Mechanism Discussion, and Application as Glucose Sensor. *Chem. Mater.* **2007**, *19*, 4174−4180.
(12) Lee, H.; Yoon, S. W.; Kim, E. J.; Park, J. In-Situ Growth of Copper Sulfide Nanocrystals on Multiwalled Carbon Nanotubes and Their Application as Novel Solar Cell and Amperometric Glucose Sensor Materials. *Nano Lett.* **2007**, *7*, 778−784.
(13) Van der Zee, F. P.; Cervantes, F. J. Impact and Application of Electron Shuttles on the Redox (Bio) Transformation of Contaminants: A Review. *Biotechnol. Adv.* **2009**, *27*, 256−277.
(14) Jortner, J.; Bixon, M. *Advances in Chemical Physics: Electron Transfer-from Isolated Molecules to Biomolecules*; J. Wiley, 1999; Part 1.
(15) Dryhurst, G.; Niki, K. *Redox Chemistry and Interfacial Behavior of Biological Molecules*; Springer Science & Business Media, 2012.
(16) Simon, P.; Gogotsi, Y. Materials for Electrochemical Capacitors. *Nat. Mater.* **2008**, *7*, 845−854.
(17) Mortimer, R. J. Electrochromic Materials. *Chem. Soc. Rev.* **1997**, *26*, 147−156.
(18) Mortimer, R. J. Organic Electrochromic Materials. *Electrochim. Acta* **1999**, *44*, 2971−2981.
(19) Park, S.; Chung, T. D.; Kim, H. C. Nonenzymatic Glucose Detection Using Mesoporous Platinum. *Anal. Chem.* **2003**, *75*, 3046−3049.
(20) Park, S.; Boo, H.; Chung, T. D. Electrochemical Non-Enzymatic Glucose Sensors. *Anal. Chim. Acta* **2006**, *556*, 46−57.
(21) Wang, C.-C.; Chen, D.-H.; Huang, T.-C. Synthesis of Palladium Nanoparticles in Water-in-Oil Microemulsions. *Colloids Surf., A* **2001**, *189*, 145−154.
(22) Keuler, J. N.; Lorenzen, L.; Sanderson, R. D.; Prozesky, V.; Przybylowicz, W. J. Characterization of Electroless Plated Palladium−silver Alloy Membranes. *Thin Solid Films* **1999**, *347*, 91−98.
(23) Chen, C.; Xie, Q.; Yang, D.; Xiao, H.; Fu, Y.; Tan, Y.; Yao, S. Recent Advances in Electrochemical Glucose Biosensors: A Review. *RSC Adv.* **2013**, *3*, 4473−4491.
(24) Wang, G.; Zhang, L.; Zhang, J. A Review of Electrode Materials for Electrochemical Supercapacitors. *Chem. Soc. Rev.* **2012**, *41*, 797−828.
(25) Jiang, J.; Li, Y.; Liu, J.; Huang, X.; Yuan, C.; Lou, X. W. D. Recent Advances in Metal Oxide-based Electrode Architecture Design for Electrochemical Energy Storage. *Adv. Mater.* **2012**, *24*, 5166−5180.
(26) Wang, J.; Thomas, D. F.; Chen, A. Nonenzymatic Electrochemical Glucose Sensor Based on Nanoporous PtPb Networks. *Anal. Chem.* **2008**, *80*, 997−1004.
(27) Xu, K.; Huang, X.; Liu, Q.; Zou, R.; Li, W.; Liu, X.; Li, S.; Yang, J.; Hu, J. Understanding the Effect of Polypyrrole and Poly(3,4-Ethylenedioxythiophene) on Enhancing the Supercapacitor Performance of $NiCo_2O_4$ Electrodes. *J. Mater. Chem. A* **2014**, *2*, 16731−16739.
(28) Lu, X.; Huang, X.; Xie, S.; Zhai, T.; Wang, C.; Zhang, P.; Yu, M.; Li, W.; Liang, C.; Tong, Y. Controllable Synthesis of Porous Nickel−Cobalt Oxide Nanosheets for Supercapacitors. *J. Mater. Chem.* **2012**, *22*, 13357−13364.
(29) Lei, Y.; Li, J.; Wang, Y.; Gu, L.; Chang, Y.; Yuan, H.; Xiao, D. Rapid Microwave-Assisted Green Synthesis of 3D Hierarchical Flower-Shaped $NiCo_2O_4$ Microsphere for High-Performance Supercapacitor. *ACS Appl. Mater. Interfaces* **2014**, *6*, 1773−1780.
(30) Wan, L.; Xiao, J.; Xiao, F.; Wang, S. Nanostructured (Co, Ni)-Based Compounds Coated on a Highly Conductive Three Dimensional Hollow Carbon Nanorod Array (HCNA) Scaffold for High Performance Pseudocapacitors. *ACS Appl. Mater. Interfaces* **2014**, *6*, 7735−7742.
(31) Militello, M. C.; Simko, S. J. Elemental Palladium by XPS. *Surf. Sci. Spectra* **1994**, *3*, 387−394.
(32) Gabasch, H.; Unterberger, W.; Hayek, K.; Klötzer, B.; Kleimenov, E.; Teschner, D.; Zafeiratos, S.; Hävecker, M.; Knop-Gericke, A.; Schlögl, R. In Situ XPS Study of Pd(111) Oxidation at Elevated Pressure, Part 2: Palladium Oxidation in the 10^{-1} Mbar Range. *Surf. Sci.* **2006**, *600*, 2980−2989.
(33) Cui, B.; Lin, H.; Liu, Y.-z.; Li, J.-b.; Sun, P.; Zhao, X.-c.; Liu, C.-j. Photophysical and Photocatalytic Properties of Core-Ring Structured $NiCo_2O_4$ Nanoplatelets. *J. Phys. Chem. C* **2009**, *113*, 14083−14087.
(34) Lee, D. U.; Kim, B. J.; Chen, Z. One-Pot Synthesis of a Mesoporous $NiCo_2O_4$ Nanoplatelet and Graphene Hybrid and Its Oxygen Reduction and Evolution Activities as an Efficient Bi-Functional Electrocatalyst. *J. Mater. Chem. A* **2013**, *1*, 4754−4762.
(35) Kong, D.; Ren, W.; Cheng, C.; Wang, Y.; Huang, Z.; Yang, H. Y. Three-Dimensional NiCo2O4@Polypyrrole Coaxial Nanowire Arrays on Carbon Textiles for High-Performance Flexible Asymmetric Solid-State Supercapacitor. *ACS Appl. Mater. Interfaces* **2015**, *7*, 21334−21346.
(36) Cheng, J.; Lu, Y.; Qiu, K.; Yan, H.; Xu, J.; Han, L.; Liu, X.; Luo, J.; Kim, J.-K.; Luo, Y. Hierarchical Core/Shell NiCo2O4@NiCo2O4 Nanocactus Arrays with Dual-Functionalities for High Performance Supercapacitors and Li-Ion Batteries. *Sci. Rep.* **2015**, *5*, 12099.
(37) Cui, C.; Xu, J.; Wang, L.; Guo, D.; Mao, M.; Ma, J.; Wang, T. Growth of NiCo2O4@MnMoO4 Nanocolumn Arrays with Superior Pseudocapacitor Properties. *ACS Appl. Mater. Interfaces* **2016**, *8*, 8568−8575.
(38) Naik, K. K.; Kumar, S.; Rout, C. S. Electrodeposited Spinel NiCo2O4 Nanosheet Arrays for Glucose Sensing Application. *RSC Adv.* **2015**, *5*, 74585−74591.
(39) Naik, K. K.; Rout, C. S. Electrodeposition of ZnCo2O4 Nanoparticles for Biosensing Applications. *RSC Adv.* **2015**, *5*, 79397−79404.
(40) Naik, K. K.; Ratha, S.; Rout, C. S. Phase and Shape Dependent Non−enzymatic Glucose Sensing Properties of Nickel Molybdate. *ChemistrySelect* **2016**, *1*, 5187−5195.
(41) Liu, S.; Hui, K. S.; Hui, K. N. Flower-like Copper Cobaltite Nanosheets on Graphite Paper as High-Performance Supercapacitor Electrodes and Enzymeless Glucose Sensors. *ACS Appl. Mater. Interfaces* **2016**, *8*, 3258−3267.
(42) Kannan, P. K.; Hu, C.; Morgan, H.; Rout, C. S. One-Step Electrodeposition of NiCo2S4 Nanosheets on Patterned Platinum Electrodes for Non-Enzymatic Glucose Sensing. *Chem.—Asian J.* **2016**, *12*, 1837−1841.
(43) Naik, K. K.; Khare, R. T.; More, M. A.; Late, D. J.; Rout, C. S. Glucose Sensing and Low-Threshold Field Emission from $MnCo_2O_4$ Nanosheets. *RSC Adv.* **2016**, *6*, 29734−29740.
(44) Kresse, G.; Hafner, J. Ab Initio Molecular Dynamics for Liquid Metals. *Phys. Rev. B: Condens. Matter Mater. Phys.* **1993**, *47*, 558.
(45) Kresse, G.; Hafner, J. Ab Initio molecular-dynamics simulation of the liquid-metal—amorphous semiconductor transition in germanium. *Phys. Rev. B: Condens. Matter Mater. Phys.* **1994**, *49*, 14251−14269.
(46) Kresse, G.; Furthmüller, J. Efficient Iterative Schemes for ab initio total-Energy Calculations Using a Plane-Wave Basis Set. *Phys. Rev. B: Condens. Matter Mater. Phys.* **1996**, *54*, 11169−11186.

DOI: 10.1021/acsami.7b02217
ACS Appl. Mater. Interfaces XXXX, XXX, XXX−XXX

(47) Kresse, G.; Furthmüller, J. Efficiency of Ab-Initio Total Energy Calculations for Metals and Semiconductors Using a Plane-Wave Basis Set. *Comput. Mater. Sci.* **1996**, *6*, 15−50.
(48) Perdew, J. P.; Burke, K.; Ernzerhof, M. Generalized Gradient Approximation Made Simple. *Phys. Rev. Lett.* **1996**, *77*, 3865−3868.
(49) Monkhorst, H. J.; Pack, J. D. Special Points for Brillouin-Zone Integrations. *Phys. Rev. B: Solid State* **1976**, *13*, 5188−5192.
(50) Bitla, Y.; Chin, Y.-Y.; Lin, J.-C.; Van, C. N.; Liu, R.; Zhu, Y.; Liu, H.-J.; Zhan, Q.; Lin, H.-J.; Chen, C.-T.; Chu, Y.-H.; He, Q. Origin of Metallic Behavior in $NiCo_2O_4$ Ferrimagnet. *Sci. Rep.* **2015**, *5*, 15201.
(51) Shi, X.; Bernasek, S. L.; Selloni, A. Formation, Electronic Structure, and Defects of Ni Substituted Spinel Cobalt Oxide: A DFT+U Study. *J. Phys. Chem. C* **2016**, *120*, 14892−14898.
(52) Modak, P.; Chakraborty, B.; Banerjee, S. Study on the Electronic Structure and Hydrogen Adsorption by Transition Metal Decorated Single Wall Carbon Nanotubes. *J. Phys.: Condens. Matter* **2012**, *24*, 185505.
(53) Chakraborty, B.; Modak, P.; Banerjee, S. Hydrogen Storage in Yttrium-Decorated Single Walled Carbon Nanotube. *J. Phys. Chem. C* **2012**, *116*, 22502−22508.
(54) Grimme, S. J. Semiempirical GGA-type density functional constructed with a long-range dispersion correction. *Comput. Chem.* **2006**, *27*, 1787−1799.

DOI: 10.1021/acsami.7b02217
ACS Appl. Mater. Interfaces XXXX, XXX, XXX−XXX